Int. J. Heat Mass Transfer. Vol. 30, No. 10, pp. 2137–2149, 1987
Printed in Great Britain

0017-9310/87 $3.00 + 0.00

Effect of external laminar channel flow on mass transfer in a cavity

HO NAM CHANG,† HWA WON RYU, DEUG HO PARK
and YONG SEOK PARK

Department of Chemical Engineering, Korea Advanced Institute of Science and Technology, P.O. Box 131, Cheongryang, Seoul, Korea

and

JOONG KON PARK

Department of Chemical Engineering, Kyungpook National University, Taegu, Korea

(*Received* 13 *October* 1986 *and in final form* 17 *March* 1987)

Abstract—To investigate the enhancement of mass transfer by vortices induced in a cavity due to external channel flow, numerical analysis has been carried out for various aspect ratios, Reynolds numbers and Schmidt numbers. As the aspect ratio increases the number of vortices increase but only the primary and the secondary vortices have such a strength as to enhance mass transfer. For each aspect ratio the mean Sherwood number was expressed in the form $Sh_m = K\,Re^x\,Sc^y$. For an aspect ratio of one, the results have been compared with experimental data measured by the limiting current method and good agreement, within an error range of 20%, was obtained.

1. INTRODUCTION

HEAT OR mass transfer between a flowing fluid and a solid surface with cavities occurs in many engineering problems. Such cavities can be found in the pores of membranes or catalyst supports, in a system of turbulence promoters, in the void space between packing materials in a packed bed, etc. It is well known that external flows induce a vortex in a cavity. This convective vortex motion promotes mass transfer between the fluid and the wall cavity, particularly when the diffusivity of the transferring species in the fluid is very small.

Many investigators have made studies of heat or mass transfer in cavities related to the application of turbulence promoters. Roshko [1] measured the pressure, velocity and friction in a rectangular cavity in the floor of a wind tunnel. Charwat *et al.* [2] proposed a mass exchange model to explain the process of heat transfer in a shallow cavity in supersonic or subsonic flow region, but this model does not seem to be adequate for deeper cavities. Haugen and Dhanak [3] studied heat transfer in turbulent flow with the conditions of uniform temperature and uniform heat flux at cavity walls. Wragg *et al.* [4] measured local wall mass transfer distributions using the electrochemical technique in circumferential cavities in pipe walls. The overall mass transfer coefficients from the cavity base decreased sharply as the cavity aspect ratio varied from 0.91 to 4.4. The mass transfer rates at the side walls upstream and downstream were quite different. Yamamoto *et al.* [5] performed experiments to measure the heat transfer characteristics in cavities with aspect ratios (AR) less than or equal to 1.0. They found that reattachment of separated flow for shallow cavities, and vortex flow for deeper ones, had a large effect on heat transfer. Aggarwal and Talbot [6] obtained local mass transfer coefficients electrochemically in a semi-cylindrical hollow to apply their results to blood oxygenation. It was shown that Sherwood number increases with both Reynolds number and the cavity hollow diameter. Berger and Hau [7] measured the mass transfer coefficient in the range of $1/10 \leqslant AR \leqslant 1/3$, $10\,000 \leqslant Re \leqslant 250\,000$ and $1000 \leqslant Sc \leqslant 7000$. They showed that the distribution of the local mass transfer coefficients along the bottom of a cavity is uniform at higher Reynolds numbers and that the values are independent of Schmidt number. Kang and Chang [8] numerically investigated the hydrodynamic performance of both cavity-type and zigzag-type turbulence promoters and proposed an empirical correlation for Sherwood number in terms of both Reynolds number and Schmidt number. Kim *et al.* [9] measured local mass transfer rates with the limiting current method and compared their results with those obtained by Kang and Chang [8] and found good agreement. Bhatti and Aung [10] made a numerical analysis on a shallow cavity of which the walls were held at a uniform temperature.

Most of the above studies have been limited to cavities of low AR. Pan and Acrivos [11], Weiss and Florsheim [12], however, investigated flow in cavities with high AR under the condition of creeping flow.

† Author to whom all correspondence should be addressed.

NOMENCLATURE

AR aspect ratio, D^*/W [—]
C dimensionless concentration [—]
C' concentration [mol cm^{-3}]
C_b bulk concentration [mol cm^{-3}]
C_{in} inlet concentration [mol cm^{-3}]
C_s concentration at electrode surface [mol cm^{-3}]
D diffusivity [cm^2 s^{-1}]
D^* depth of cavity [cm]
F Faraday constant [C mol^{-1}]
i_{lim} limiting current density [A cm^{-2}]
k mass transfer coefficient [cm s^{-1}]
K constant [—]
L characteristic length, D^* [cm]
N_Y mass flux in Y-direction [mol cm^{-2} s^{-1}]
Pe Peclet number, $\bar{U}W/D$ [—]
Re Reynolds number, $\rho\bar{U}W/\mu$ [—]
Sh Sherwood number, kL/D [—]
Sh_m mean Sherwood number defined in equation (16) [—]
U X-component of a dimensionless velocity [—]
V Y-component of a dimensionless velocity [—]
W width of a cavity [cm]
Y^* normalized dimensionless coordinate Y, Y/AR [—]
z number of electrons exchanged during electrode reaction [—].

Greek symbols
λ constant for convergence criterion [—]
μ viscosity [g cm^{-1} s^{-1}]
ρ density of a fluid [g cm^{-3}]
φ general dependent variable [—]
ψ dimensionless stream function [—]
ω dimensionless vorticity [—].

Superscripts
$'$ dimensional quantity
N iteration number.

Subscripts
i ith node in X-coordinate
j jth node in Y-coordinate
s solid wall.

They showed that successive secondary vortices exist, and that the strength of the vortices decreases rapidly. Therefore, it is expected that the effect of the vortices induced in a cavity on mass transfer also decreases as AR increases.

The present study is concerned with mass transfer between a fluid and a cavity which has an active bottom wall. The maximum values in the present investigation are 300 for Re, 10000 for Sc and 10 for AR. A numerical study and mass transfer experiments using the limiting current method have been performed and comparisons between the results have been made.

2. GOVERNING EQUATIONS AND NUMERICAL ANALYSIS

A schematic diagram of a rectangular cavity is shown in Fig. 1. The width of the cavity is the same as the distance between the rectangular channel plates. The aspect ratio is defined as the ratio of the height to the width of the cavity. The inlet upstream flow of the channel is assumed to be a fully developed laminar flow. The concentration of the inlet fluid is assumed to be uniform and the walls are assumed to be inert except the cavity bottom wall at which zero concentration is assumed. The following equations need to be solved in order to obtain the velocity and concentration profiles in the field: (i) equation of motion in the X-direction; (ii) equation of motion in the Y-direction; (iii) continuity equation; (iv) mass transfer equation. For a dilute solution it may be assumed that concentration does not significantly affect the properties of the fluid. Therefore, the flow field can be obtained from equations (i), (ii) and (iii). The solution of the stream function is used to solve equation (iv). To simplify the governing equations, the following dimensionless variables are introduced:

$$X = X'/W, \quad Y = Y'/W, \quad \psi = \psi'/\bar{U}W,$$
$$\omega = \bar{U}\omega'/W, \quad C = C'/C_{in}$$
$$Re = \rho\bar{U}W/\mu, \quad Sc = \mu/\rho D, \quad Pe = Re\,Sc = \bar{U}W/D. \tag{1}$$

The simplified governing equations using the above

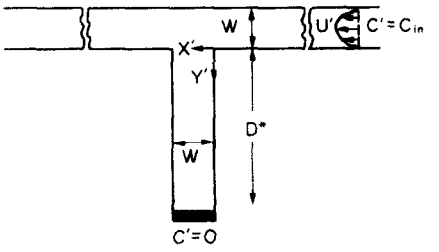

FIG. 1. Model of mass transfer in a cavity.

dimensionless variables are as follows:

$$\nabla^2\psi = -\omega \tag{2}$$

$$\nabla^2\omega = Re\left(\frac{\partial\psi}{\partial Y}\frac{\partial\omega}{\partial X} - \frac{\partial\psi}{\partial X}\frac{\partial\omega}{\partial Y}\right) \tag{3}$$

$$\nabla^2 C = Pe\left(\frac{\partial\psi}{\partial Y}\frac{\partial C}{\partial X} - \frac{\partial\psi}{\partial X}\frac{\partial C}{\partial Y}\right). \tag{4}$$

The boundary conditions are:

(i) at $X = -5$ (inlet of the channel)

$$\frac{\partial\psi}{\partial X} = \frac{\partial\omega}{\partial X} = 0, \quad C = 1; \tag{5}$$

(ii) at $X = 25$ (outlet of the channel)

$$\frac{\partial\psi}{\partial X} = \frac{\partial\omega}{\partial X} = \frac{\partial C}{\partial X} = 0; \tag{6}$$

(iii) at $Y = -1$ (upper wall of the channel)

$$\psi = -1, \quad \frac{\partial\psi}{\partial X} = \frac{\partial\psi}{\partial Y} = \frac{\partial C}{\partial Y} = 0; \tag{7}$$

(iv) at $X = 0$, $0 \leqslant Y \leqslant AR$ (side wall of the cavity)

$$\psi = 0, \quad \frac{\partial\psi}{\partial X} = \frac{\partial\psi}{\partial Y} = \frac{\partial C}{\partial X} = 0; \tag{8}$$

(v) at $y = AR$, $0 \leqslant X \leqslant 1$
(bottom wall of the cavity)

$$\psi = 0, \quad \frac{\partial\psi}{\partial X} = \frac{\partial\psi}{\partial Y} = 0, \quad C = 0; \tag{9}$$

(vi) at all the other walls

$$\psi = 0, \quad \frac{\partial\psi}{\partial X} = \frac{\partial\psi}{\partial Y} = \left(\frac{\partial C}{\partial n}\right)_s = 0; \tag{10}$$

where n stands for the distance from the wall along the normal.

The upwind difference method developed by Gosman *et al.* [13] has been used by transforming the governing equations into the following form:

$$a_\varphi\left\{\frac{\partial}{\partial X}\left(\frac{\partial\psi}{\partial Y}\right) - \frac{\partial}{\partial Y}\left(\varphi\frac{\partial\psi}{\partial X}\right)\right\} - \left[\frac{\partial}{\partial X}\left\{b_\varphi\frac{\partial}{\partial X}(c_\varphi\psi)\right\} + \frac{\partial}{\partial Y}\left\{b_\varphi\frac{\partial}{\partial Y}(c_\varphi\psi)\right\}\right] + d_\varphi = 0 \tag{11}$$

where ψ denotes the dependent variables and a_φ, b_φ, c_φ, and d_φ are coefficients the values of which are listed in Table 1. In order to obtain the vorticity at the wall, the assumption of the linear variation of vorticity from the wall to the neighbouring point is used. Detailed procedures for the solution can be found elsewhere [8, 13].

Table 1. Coefficients of equation (11)

	a_φ	b_φ	c_φ	d_φ
ω	1	1	$1/Re$	0
ψ	0	1	1	$-\omega$
C	1	$1/Pe$	1	0

Because the gradients of the velocity or concentration are expected to be large near the walls or near the shear layer at the open side of the cavity, a variable grid is used giving high density at these regions. The mesh size ranges from $h = 1/200$ near the wall to 5 downstream of the channel. The number of grids has been increased with AR, namely, 45×30 when $AR = 1$ and 45×43 when $AR = 10$. Typical grid points are listed in Table 2.

As a convergence criterion, equation (12) is used when the value at each grid is very close to zero. Otherwise equation (13) is adopted

$$\left|\frac{\psi_{i,j}^{(N)} - \psi_{i,j}^{(N-1)}}{\psi_{\max}^{(N-1)}}\right|_{\max} = \lambda_1 \tag{12}$$

$$\left|\frac{\psi_{i,j}^{(N)} - \psi_{i,j}^{(N-1)}}{\psi_{i,j}^{(N)}}\right|_{\max} = \lambda_2 \tag{13}$$

where λ_1 has been taken to be 10^{-6}–10^{-5} and λ_2 to be 5×10^{-5}. When AR is small, equation (12) is sufficient to give a converged solution. But when AR becomes larger, the order of magnitude of the stream function near the bottom of the cavity is much smaller than λ_1 and equation (12) is insufficient as a convergence criterion. In cases when equation (13) alone is used as a convergence criterion, fluctuations may occur near the boundaries between vortices that have very small values with sign change. Thus, at the beginning we proceed under the criterion of equation (12) and then change the criterion to equation (13) to obtain a converged error.

For stable solutions the under-relaxation method has been used for the calculation of vorticity at the expense of long computation time. From our experience, relaxation parameters of 0.2 for the calculation of vorticity, 1.4 for the stream function, and 1.1–1.3 for the concentration were used.

The parameters considered in this study are as follows:

AR: 1, 3, 5, 7, 10

Re: 0.1, 1, 10, 100, 300

Sc: 1, 10, 100, 1000, 1655, 10 000.

The rate of mass transfer at the bottom of a cavity is as follows:

$$N_Y = -D\left(\frac{\partial C'}{\partial Y'}\right)_s = kL(C'_{in} - C'_s). \tag{14}$$

In dimensionless form

$$Sh = \frac{kL}{D} = -AR\left(\frac{\partial C}{\partial Y}\right)_{Y=AR}. \tag{15}$$

Table 2. Grid points ($AR = 1$)

X	−5	−4	−3	−2	−1.5	−1	−0.5	−0.25	−0.1
	0	0.005	0.01	0.02	0.05	0.1	0.15	0.32	0.3
	0.4	0.5	0.6	0.7	0.8	0.85	0.9	0.95	0.98
	0.99	0.995	1	1.05	1.1	1.3	1.6	2	2.5
	3	4	5	7	9	12	15	20	25
Y	−1	−0.95	−0.9	−0.8	−0.7	−0.5	−0.3	−0.2	−0.1
	−0.05	0	0.05	0.1	0.15	0.2	0.3	0.4	0.5
	0.6	0.7	0.8	0.85	0.9	0.93	0.96	0.98	0.985
	0.99	0.995	1						

The mean Sherwood number is defined as

$$Sh_m = \int_0^1 Sh \, dX. \tag{16}$$

3. EXPERIMENT

3.1. *Limiting current method*

The limiting current method is a convenient technique for the measurement of local mass transfer. The method is based on the redox reaction of ferri- and ferrocyanide in an excess of a carrier electrolyte such as sodium hydroxide. A detailed discussion of the limiting current technique can be found elsewhere [14, 15].

The mass transfer coefficient at the cathode surface is calculated from the following equation with $z = 1$ and $C_s = 0$:

$$k = \frac{i_{lim}}{zF(C_b - C_s)}. \tag{17}$$

The rate of mass transfer can be expressed in a dimensionless form as

$$Sh = \frac{kL}{D} = \frac{i_{lim}L}{zFC_bD} \tag{18}$$

where L is a characteristic length and represents the depth of a cavity in the present system. Since the variables such as D, F, L and z are given and C_b can be obtained by analysis of the solution, the mass transfer coefficient can easily be determined from the above equation.

3.2. *Experimental apparatus*

A schematic diagram of the experimental apparatus is shown in Fig. 2. The electrolyte is pumped from a reservoir through a flow damper, thermostat, flowmeter and, finally, into the test cell. The flow damper is installed to prevent gas bubbles from entering the test cell and to relax the pulsation generated by the pump. The temperature of the solution is controlled at $25 \pm 0.5°C$. The flow rate is measured by a calibrated float-type meter. Nitrogen is bubbled through the solution in the reservoir to remove dissolved oxygen. Details of the test cell are presented in Fig. 3. The cavity is placed 60 cm behind the entrance to the test cell in order to satisfy the fully developed flow condition. The cathode is placed at the bottom of the cavity and the anode (2×10 cm) is placed 20 cm downstream of the cavity. The height and the width of the channel are 2 and 10 cm, respectively, and those of the cavity are both 2 cm. The span of the cavity is 10 cm and all of the span is used as the cathode but measurements have been made only at the central 3 cm. The measuring cathode is divided into six smaller electrodes separated by insulating epoxy resin

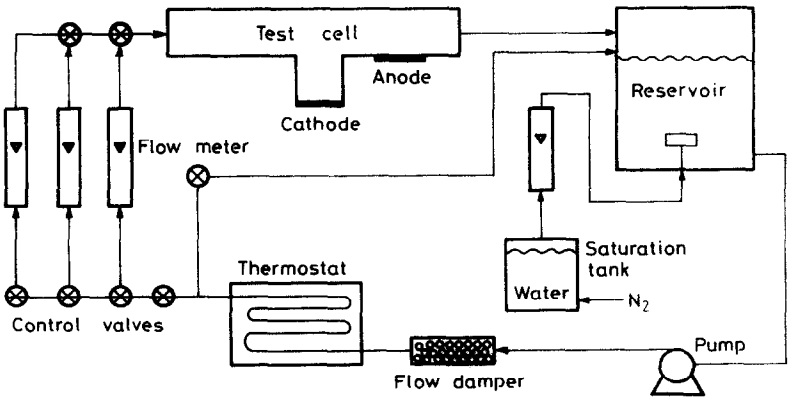

FIG. 2. Schematic diagram of experimental equipment.

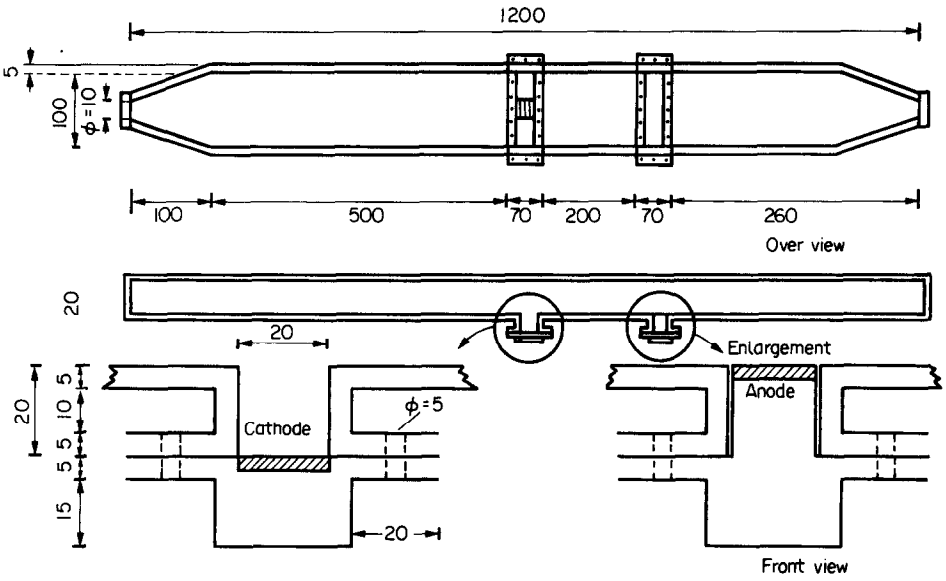

FIG. 3. Details of the test cell.

and the total electrode area amounts to 68.0% of the total cathode area. The electrodes are polished with fine emery paper and then wiped with CCl_4.

To activate the cathodes, 5 V is applied to them in reverse polarity in 2N NaOH solution for 5 min. The electric circuit used to measure currents is similar to that described elsewhere [9].

3.3. *Measurement of the current*

Typical polarization curves were obtained for various *Re* up to 300 and limiting currents were obtained at above 400 mV. A constant voltage of 700 mV was supplied using a d.c. power supplier. The voltage and the current are measured by a digital multimeter (Model 616 and 619, Keithley). When the currents fluctuated, they were passed through a resistor and the voltage drops were monitored on a chart recorder.

4. RESULTS AND DISCUSSIONS

4.1. *Fow field and concentration profile*

A typical velocity profile at the centre of the cavity of $AR = 1$ is shown in Fig. 4. As *Re* decreases, the point of $U = 0$ moves downward. This means that the external flow penetrates more deeply into the cavity as the velocity decreases. The maximum value of the stream function in a vortex is given in Fig. 5. As *Re*

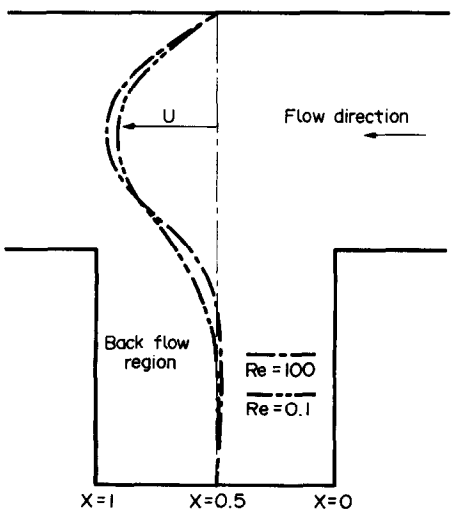

FIG. 4. Profile of X-direction velocity at cavity centre.

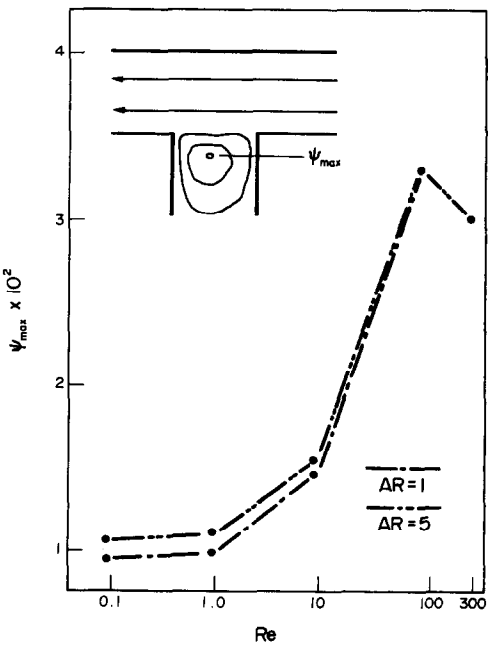

FIG. 5. Maximum value of the stream function.

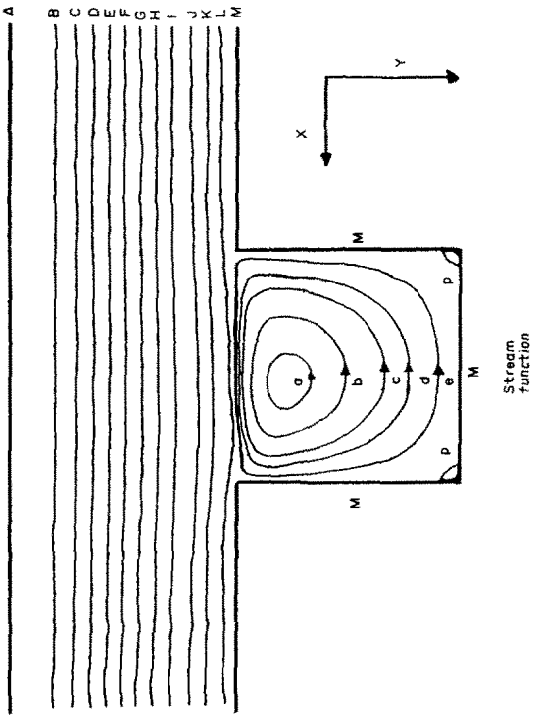
A
B C D E F G H I J K L M
X
Y
M
a b c d e
p
Stream function

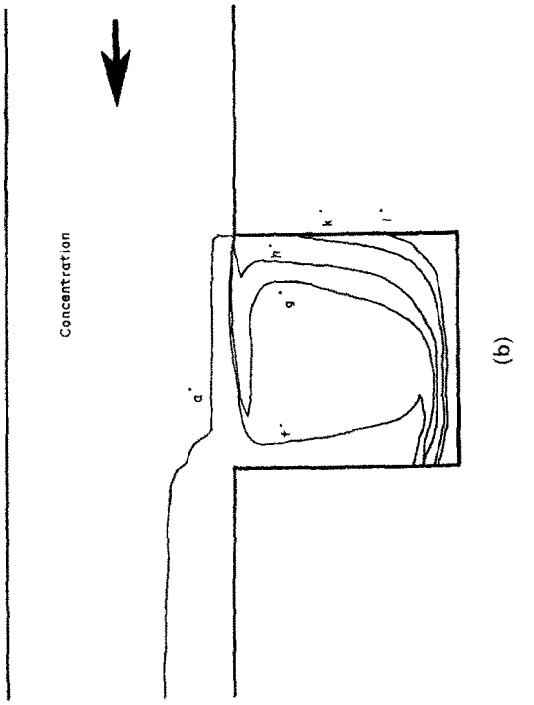
Concentration
a' f' g' h' k' l'
(b)

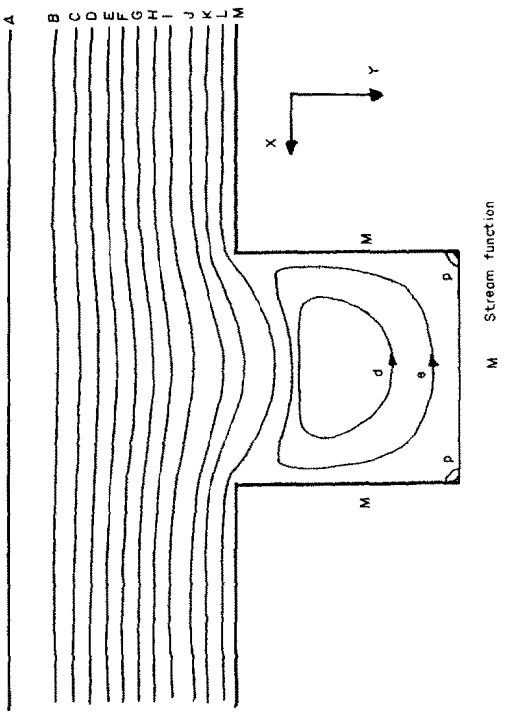
A
B C D E F G H I J K L M
X
Y
M
d e
p
M Stream function

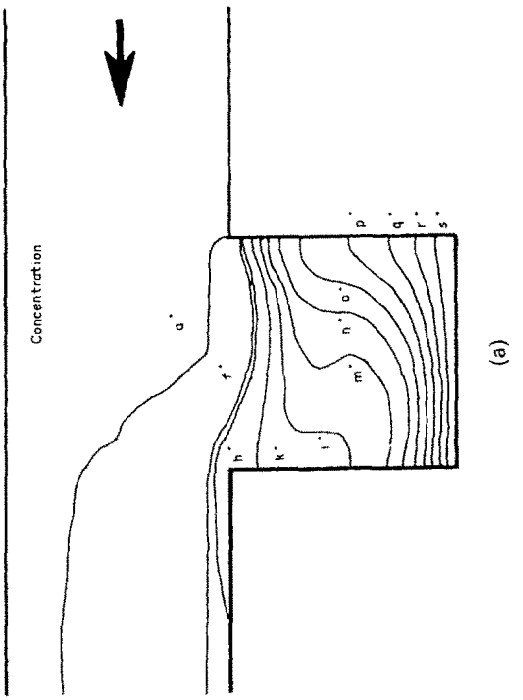
Concentration
a' f' h' k' l' m' n' o' p' q' r' s'
(a)

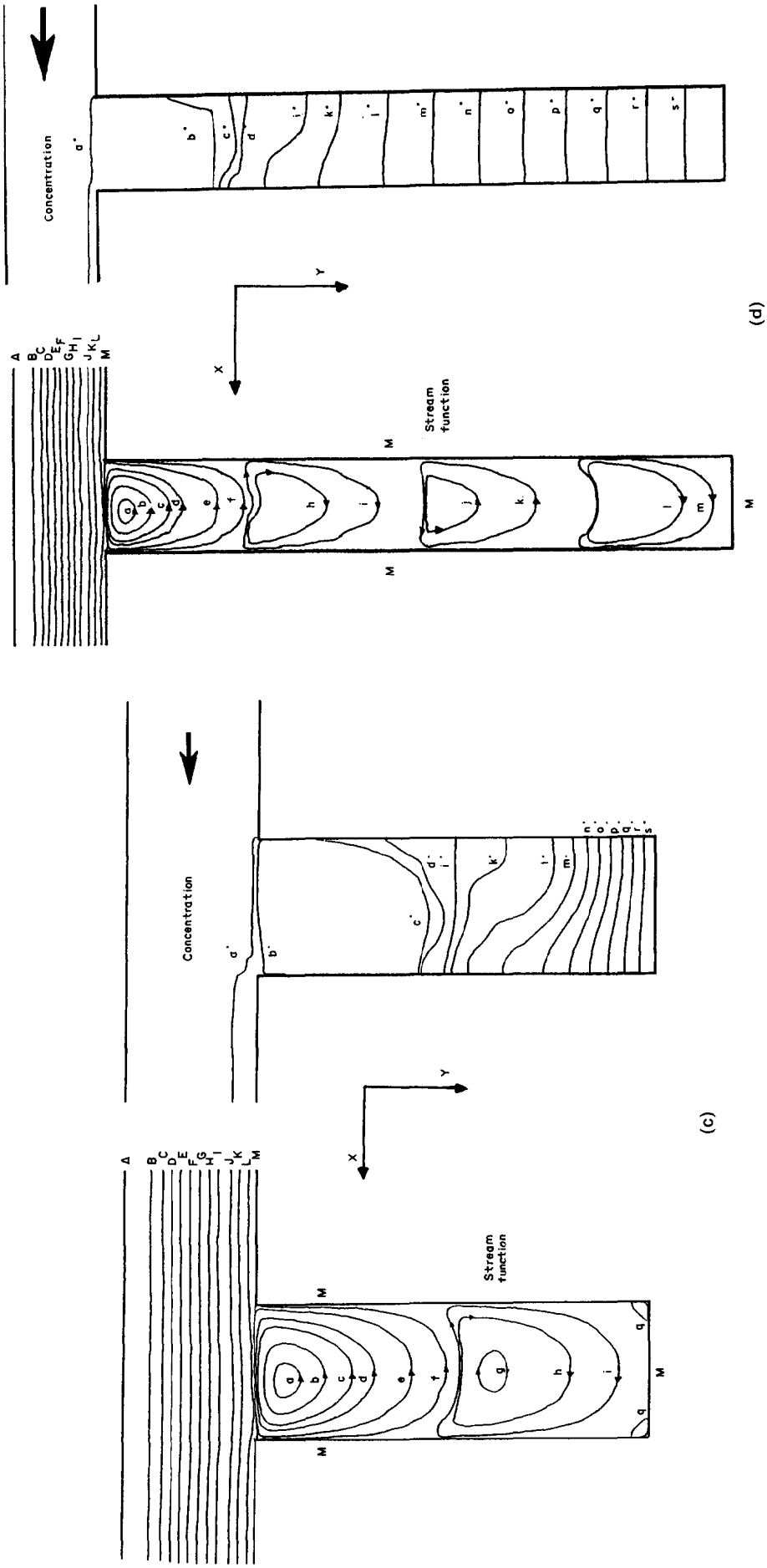

FIG. 6. Contours of stream function and contours of concentration ($Sc = 1000$): (a) $AR = 1$, $Re = 1$; (b) $AR = 1$, $Re = 100$; (c) $AR = 3$, $Re = 100$; (d) $AR = 7$, $Re = 100$.

increases ψ_{max} also increases to a maximum value at around $Re = 100$. As Re increases, the location of ψ_{max} moves downward due to inertial forces. Then the gradient of ψ between the wall at which $X = 1$ and the lane at which ψ_{max} lies increases because of the shorter distance between the two planes. To conserve the total mass flow rate between the two planes ψ_{max} should decrease at Re higher than 100.

Sample contour maps of the streamlines and concentrations are shown in Figs. 6(a)–(d) and the values of the symbols in the figures are given in Table 3. When AR is 1.0 (Figs. 6(a) and (b)), the vortex centre shifts downstream as Re increases and thus the streamlines between the vortex centre and the plane at $X = 1$ are denser than the streamlines between the vortex centre and the plane at $X = 0$. This means that the magnitude of the downstream vertical velocity is larger than the upstream one. The concentration contour lines show that the concentration changes rapidly near the bottom of the cavity at higher Re. The equi-concentration lines penetrate more deeply toward the bottom of the cavity at the downstream side so that the maximum local mass transfer rate is expected at this region. The number of recirculating vortices at $Re = 100$ increases to 2, 3, 4, and 5 as AR increases to 3, 5, 7, and 10, respectively (Figs. 6(c) and (d)). The directions of rotation change alternately as the number of vortices increase. When $AR = 3$, the equi-concentration lines of the primary vortex penetrate more deeply at the downstream side while those of the secondary vortex penetrate at the upstream side due to the change of direction of rotation. The concentration contour maps of AR greater than 5 are nearly parallel to the X-axis except in the region of the primary and secondary vortices. This means that only the primary and secondary vortices have enough strength to influence the mass transfer and the effects of other vortices on mass transfer are insignificant.

Table 3. The values of constant line in Fig. 6(c)

Position	Stream function Symbol	Value	Concentration Symbol	Value
	A	-1	a^*	0.99999
	B	-0.9	b^*	0.999
	C	-0.8	c^*	0.995
	D	-0.7	d^*	0.99
	E	-0.6	e^*	0.987
	F	-0.5	f^*	0.98
Channel flow	G	-0.4	g^*	0.978
	H	-0.3	h^*	0.97
	I	-0.2	i^*	0.95
	J	-0.1	j^*	0.92
	K	-0.05	k^*	0.9
	L	-0.01	l^*	0.8
	M	0	m^*	0.7
			n^*	0.6
	a	3×10^{-2}	o^*	0.5
	b	2×10^{-2}	p^*	0.4
1st	c	1×10^{-2}	q^*	0.3
Vortex	d	5×10^{-3}	r^*	0.2
	e	1×10^{-3}	s^*	0.1
	f	1×10^{-4}		
	g	-5×10^{-5}		
2nd	h	-1×10^{-5}		
Vortex	i	-1×10^{-6}		
3rd	j	1×10^{-8}		
Vortex	k	1×10^{-9}		
4th	l	-1×10^{-12}		
Vortex	m	-1×10^{-13}		
5th	n	1×10^{-16}		
Vortex	o	1×10^{-17}		
Small corner	p	-1×10^{-4}		
vortex	q	1×10^{-6}		

The mean concentration along the Y-axis is defined as follows:

$$\bar{C}(Y) = \frac{\int_0^1 C(X, Y)\,dX}{\int_0^1 dX}. \tag{19}$$

Substituting $Y^* = Y/AR$ into equation (15) and rewriting equation (16) with equation (19) we have

$$Sh_m = \left(\frac{d\bar{C}(Y^*)}{dY^*}\right)_{Y^*=1}. \tag{20}$$

The above equation shows that the gradient of the mean concentration at $Y^* = 1$ is the mean Sherwood number. In Fig. 7(a) $\bar{C}(Y^*)$ vs Y^* is plotted. The horizontally flat part of the curve represents the region where the primary vortex dominates. The rate of mass transfer in the Y-direction may be expressed as

$$N = CV - D\frac{dC}{dY}. \tag{21}$$

Because the primary vortex has large values of V ($CV \gg D\,dC/dY$), it has a large influence on mass transfer. The straight line which connects the points (0, 1) and (1, 0) represents pure diffusional mass transfer. As the concentration of the upstream channel is taken as a reference concentration, the mean concentration at the top of a cavity, $\bar{C}(0)$, is less than 1.0. Figure 7(b) shows that $\bar{C}(Y^*)$ has lower values at higher AR. Because the relative size of the primary vortex is inversely proportional to AR, the flat part of $\bar{C}(Y^*)$ is smaller as AR increases. The inflection points indicate that the secondary eddies also have influences on mass transfer. As AR increases the effect of the secondary vortex decreases gradually not only due to its relatively small size but also its smaller strength. Pure diffusional mass transfer occurs in the region where $\bar{C}(Y^*)$ decreases linearly. Figures 7(a) and (b) clearly show that only the primary and secondary vortices affect mass transfer and the higher numbered vortices have a negligible effect on mass transfer.

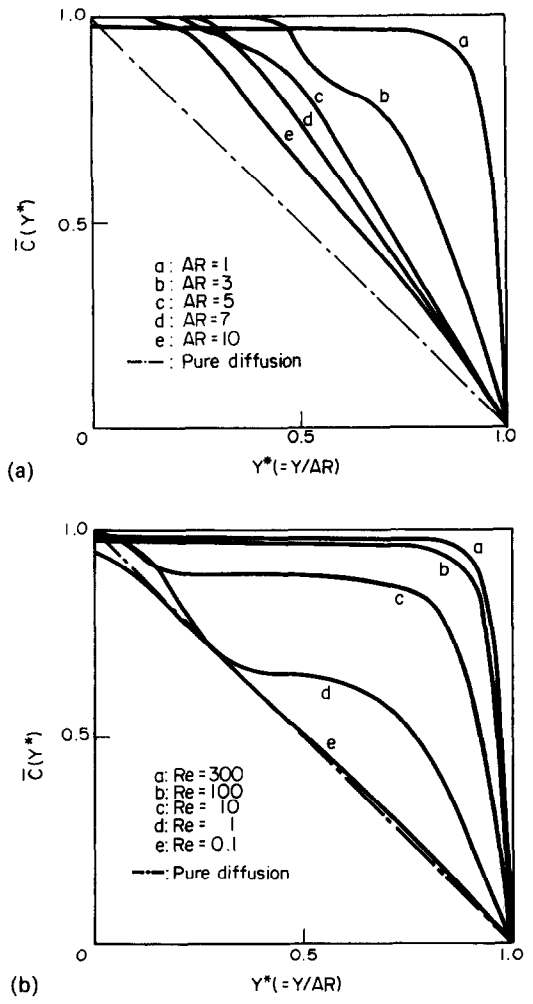

FIG. 7. Mean concentration profile along Y^*: (a) Reynolds number is varied ($AR = 1$, $Sc = 1000$); (b) aspect ratio is varied ($Re = 100$, $Sc = 1000$).

4.2. *Distribution of local Sherwood number*

The distribution of local Sherwood number vs Re at $AR = 1$ and $Sc = 1000$ is presented in Fig. 8(a). The curves show a maximum towards the right because the fresh solution meets the bottom of a cavity near $X = 0.7$–0.8. Inflections appear near $X = 0.1$ and 0.9 owing to the small secondary vortices. At high Reynolds number, both the magnitude and deviation of local Sherwood number from those of $Re = 1$ and 0.1 increase.

The effect of Sc on mass transfer is shown in Fig. 8(b). As Sc increases, the mass transfer rate also increases and the variation of the curve becomes greater showing a larger effect of the convectional flow on mass transfer. When Sc is small, the role of diffusion becomes greater so that the curve becomes more linear.

The variation of the local Sherwood number at various AR is shown in Fig. 8(c). The maximum point for $AR = 3$ appears at the other side of the cavity in comparison with that for $AR = 1$ because of the direction of rotating of the secondary vortex. This figure also indicates that the local Sherwood number at the bottom of a cavity of AR higher than 5 is independent of X position. However, the Sherwood number is still higher than the value 1.0 corresponding to pure diffusion.

4.3. *Mean Sherwood number*

The local Sherwood number has been integrated using equation (16) and the result for $Sc = 1000$ is shown in Fig. 9. The mean Sherwood number increases with Re and the increase is higher at lower AR. When Sc is 10 000, the behaviour is similar though the magnitude of Sherwood number is increased. The mean Sherwood number can be expressed by the following equation at each AR:

$$Sh_m = K\, Re^x\, Sc^y \tag{22}$$

where K, x, and y are constants obtained from multilinear regression methods and the values are given in Table 4. The range of application of the above equation is $0.1 \leqslant Re \leqslant 300$, $1000 \leqslant Sc \leqslant 10\,000$. The coefficient K increases rapidly between $AR = 3$ and 5 and the powers x and y decrease approximately exponentially. This means that the fraction of the diffusion-controlled region increases as AR increases. The Sherwood number at high AR can be expressed as a function of Peclet number from the fact that the values of x and y approach the same value.

4.4. *Comparison of experiment with numerical analysis*

To confirm the results from the numerical analysis, mass transfer experiments were carried out for $AR = 1$, $5 \leqslant Re \leqslant 300$. Figure 10 shows the comparison of Sherwood numbers from the numerical analysis and from the experiment. The distributions of Sh agree reasonably well. It is known that the local concentrations near the insulation between the cathodes have high values due to the non-conducting region of the cathodes where the condition $C = 0$ is not satisfied. Moreover, it is also known that the effect of the non-conducting region increases at lower Re [19]. Edge effects due to electrode insulation give larger deviations in the corners when secondary eddies with small velocity occur.

The mean Sherwood numbers obtained from the experiment and from the numerical analysis are compared in Fig. 11. In the range $10 \leqslant Re \leqslant 300$ there is

Table 4. The constants in equation (22)

AR	K	x	y
1	0.2156	0.4094	0.3733
3	0.3420	0.2056	0.2033
5	0.7172	0.0837	0.0841
7	0.8191	0.0589	0.0572
10	0.8652	0.0467	0.0428

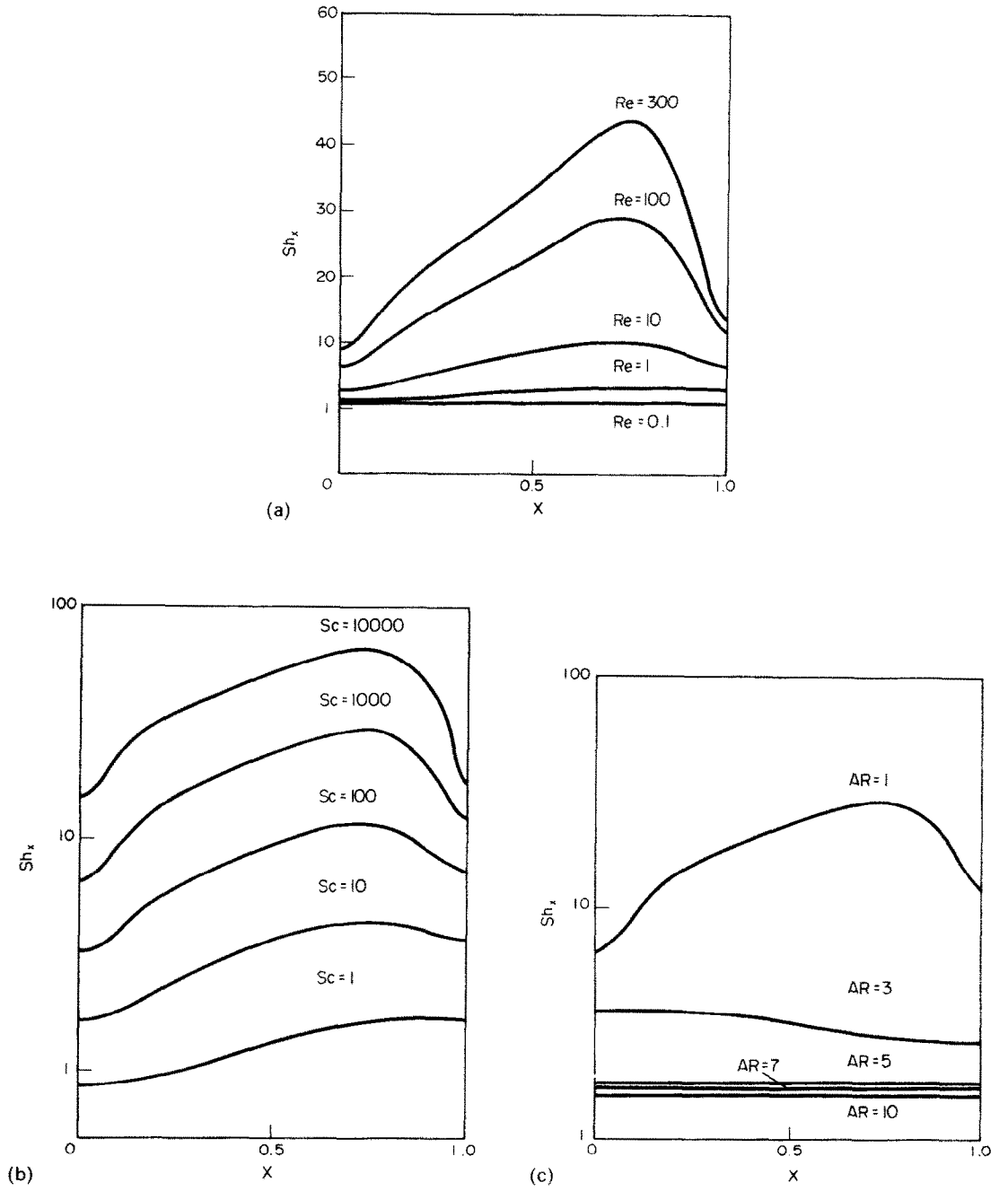

FIG. 8. Distribution of local Sherwood number at the bottom of a cavity: (a) Reynolds number is varied ($AR = 1$, $Sc = 1000$); (b) Schmidt number is varied ($AR = 1$, $Re = 100$); (c) aspect ratio is varied ($Re = 100$, $Sc = 1000$).

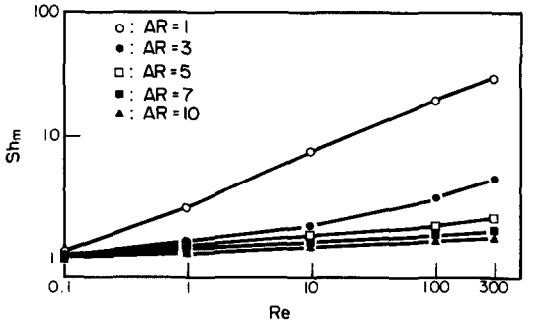

FIG. 9. Mean Sherwood number at $Sc = 1000$.

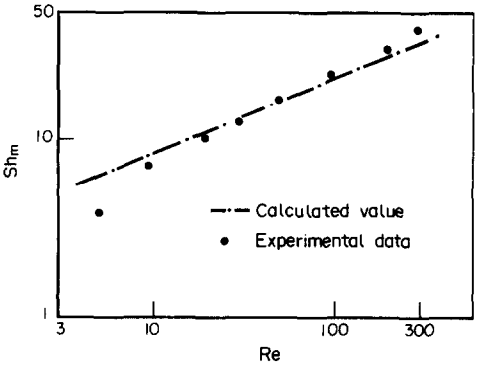

FIG. 11. Comparison of calculated values with experimental data for mean Sherwood number at $AR = 1$ and $Sc = 1655$.

agreement within 20%. When $Re = 5$ the error is about 70%. This large deviation is attributed to the effect of inert regions adjacent to the cathodes at this low Re and the long experimental time of about 10 h to attain steady state. Sutey and Knudsen [20] investigated the activity of nickel electrodes and showed deactivation of the electrode after 175 min. In this experiment the depth of the cavity was 2 cm. As can be seen in Fig. 7, the diffusion dominance region becomes larger when Re is low. To calculate the approximate time to attain steady state at extremely low Re, it is assumed that only diffusional mass transfer occurs within a cavity. Then the solution can easily be obtained as follows [21] :

$$\frac{C-C_0}{C_s-C_0}(Y,t) = \frac{Y}{L} + \sum_{n=0}^{\infty} \frac{2}{n\pi}(-1)^n \sin\left(\frac{n\pi Y}{L}\right) \times \exp(-n\pi^2 Dt/L^2) \quad (23)$$

where L is the depth of a cavity and C the concentration at the entrance (namely, $Y = 0$) of the cavity. The Sherwood number can be obtained from the following equation :

$$Sh = 1 + 2\sum_{n=0}^{\infty}(-1)^n \cos(n\pi)\exp(-n\pi^2 Dt/L^2). \quad (24)$$

The first term, 1.0, is the Sherwood number at steady state when only pure diffusion occurs. About 30 h are required to attain $Sh = 1.2$. Therefore, experiments in the cases where Re is less than 5 and AR is greater than 1 were abandoned due to the excessive time required for the steady state.

5. CONCLUSIONS

A numerical analysis has been carried out to investigate mass transfer in rectangular cavities due to external laminar flow, cavities of aspect ratio (AR between 1 and 10) being used. Experiments were car-

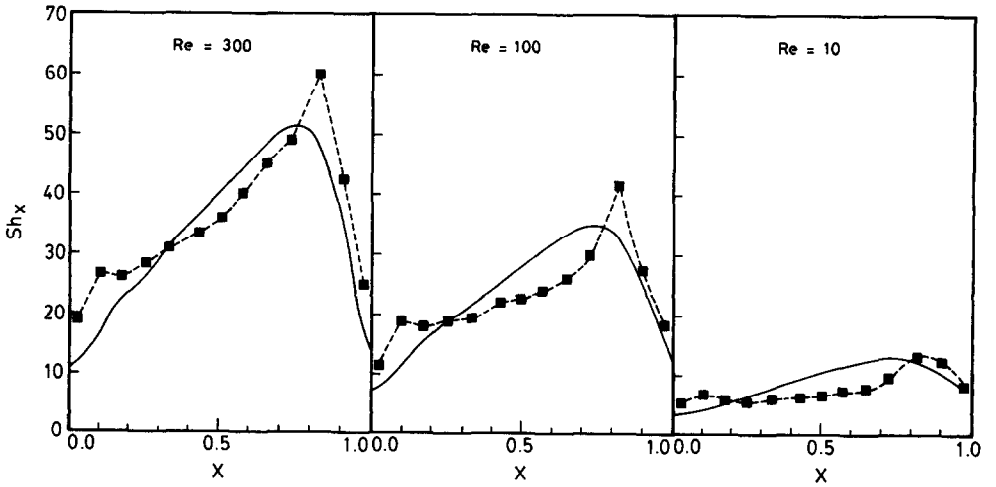

FIG. 10. Comparison of calculated values with experimental data for local Sherwood number at $AR = 1$ and $Sc = 1655$: ——, calculated; —■—, experimental.

ried out for $AR = 1$ using the limiting current method and the following conclusions were drawn.

(1) As AR increases the number of vortices also increases but the strength of the vortices reduces rapidly.

(2) Only the primary and secondary vortices have a large enough strength to promote mass transfer.

(3) Mean Sherwood number increases with both Re and Sc and can be expressed in the form $Sh_m = K\,Re^x\,Sc^y$ for each AR.

(4) The mean Sherwood number from the experiments and the numerical analysis were in agreement within about 20%.

REFERENCES

1. A. Roshko, Some measurements of flow in a rectangular cutout, *NACA TN* 3488 (1955).
2. A. F. Charwat, J. N. Roos, F. C. Dewey, Jr. and J. A. Hitz, An investigation of separated flows—Part 2. Flow in cavity and heat transfer, *J. Aerospace Sci.* **28,** 457–470 (1961).
3. R. L. Haugen and A. M. Dhanak, Heat transfer in turbulent boundary-layer separation over a surface cavity, *Trans. Am. Soc. Mech. Engrs*, Series C, *J. Heat Transfer* **89,** 335–340 (1967).
4. A. A. Wragg, M. A. Patrick, D. J. Tagg, A. R. Downey and A. J. Neilson, The use of electrochemical techniques in three fluid-flow and mass transfer studies, *Proc. Euromech 90*, Nancy, France, July (1977).
5. H. Yamamoto, N. Seki and S. Fukusako, Forced convection heat transfer on heated bottom surface of a cavity, *Trans. Am. Soc. Mech. Engrs*, Series C, *J. Heat Transfer* **101,** 475–479 (1979).
6. J. K. Aggarwal and L. Talbot, Electro-chemical measurement of mass transfer in semi-cylindrical hollows, *Int. J. Heat Mass Transfer* **22,** 61–75 (1979).
7. F. P. Berger and F. L. Hau, Local mass/heat transfer on surfaces roughened with small square ribs, *Int. J. Heat Mass Transfer* **22,** 1645–1656 (1979).
8. I. S. Kang and H. N. Chang, The effect of turbulence promoters on mass transfer—numerical analysis and flow visualization, *Int. J. Heat Mass Transfer* **25,** 1167–1181 (1982).
9. D. H. Kim, I. H. Kim and H. N. Chang, Experimental study of mass transfer around a turbulence promoter by the limiting current method, *Int. J. Heat Mass Transfer* **26,** 1007–1016 (1983).
10. A. Bhatti and W. Aung, Finite difference analysis of laminar separated forced convection in cavities, *Trans. Am. Soc. Mech. Engrs*, Series C, *J. Heat Transfer* **106,** 49–54 (1984).
11. F. Pan and A. Acrivos, Steady flows in rectangular cavities, *J. Fluid Mech.* **28,** 643–655 (1967).
12. R. F. Weiss and B. H. Florsheim, Flow in a cavity at low Reynolds number, *Physics Fluids* **8,** 1631–1635 (1965).
13. A. D. Gosman, W. M. Pun, A. K. Runchal, D. B. Spalding and M. Wolfshtein, *Heat and Mass Transfer in Recirculating Flows*. Academic Press, New York (1969).
14. P. J. Pickett, *Electrochemical Reactor Design*, 2nd Edn. Elsevier, New York (1977).
15. J. Newman, *Advances in Electrochemistry and Electrochemical Engineering*, Vol. 5. Wiley, New York (1976).
16. I. M. Kolthoff and E. A. Pearson, Stability of potassium ferrocyanide solutions, *Ind. Engng Chem. Analyt.* **3,** 381–382 (1931).
17. S. Jimori, *Z. anorg. allg. Chem.* **167,** 145 (1927).
18. L. Gordon, J. S. Newman and C. W. Tobias, The role of ionic migration in electrolytic mass transport : diffusivities of $Fe(CN)_6^{3-}$ and $Fe(CN)_6^{4-}$ in KOH and NaOH solutions, *Ber. Bunsen. Phys. Chem.* **70,** 414–420 (1966).
19. H. N. Chang, J. K. Park and C. Kim, Effect of inert regions on local mass transfer rate measurements using the limiting diffusion current technique—case of Poiseuille type flow, *Int. J. Heat Mass Transfer* **27,** 1922–1925 (1985).
20. A. M. Sutey and J. K. Knudsen, Effect of dissolved oxygen on the redox method for the measurement of mass transfer coefficients, *I&EC Fund.* **6,** 132–139 (1967).
21. V. G. Jenson and G. V. Jeffreys, *Mathematical Methods in Chemical Engineering*, 2nd Edn, pp. 284–285. Academic Press, New York (1977).

EFFET DE L'ECOULEMENT LAMINAIRE EXTERNE SUR LE TRANSFERT DE MASSE DANS UNE CAVITE

Résumé—Pour étudier l'accroissement du transfert de masse par tourbillonnement induit dans une cavité par un écoulement externe, une analyse numérique est faite pour différents rapports de forme, différents nombres de Reynolds et de Schmidt. Quand le rapport de forme augmente, le nombre de tourbillons augmente, mais seuls les tourbillons primaire et secondaire ont une intensité telle que le transfert de masse est augmenté. Pour chaque rapport de forme, le nombre de Sherwood moyen est exprimé sous la forme $Sh_m = K\,Re^x\,Sc^y$. Pour un rapport de forme unité, les résultats sont comparés avec les résultats expérimentaux déterminés par la méthode électrochimique et un bon accord est obtenu avec un écart inférieur à 20%.

EINFLUSS EINER EXTERNEN, LAMINAREN KANALSTRÖMUNG AUF DEN STOFFTRANSPORT IN EINEM HOHLRAUM

Zusammenfassung—Um die Steigerung des Stofftransports durch Verwirbelungen, die durch eine externe Kanalströmung in Hohlräumen entsteht, zu untersuchen, wurden für verschiedene Seitenverhältnisse, Schmidt- und Reynoldszahlen numerische Berechnungen durchgeführt. Mit zunehmendem Seitenverhältnis steigt die Zahl der Wirbel, aber nur die ersten beiden Wirbel sind stark genug, um den Stofftransport zu erhöhen. Für jedes Seitenverhältnis wurde die mittlere Sherwoodzahl gemäß folgender Formel berechnet: $Sh_m = K\,Re^x\,Sc^y$. Für das Seitenverhältnis Eins wurden die Ergebnisse mit experimentell ermittelten Werten verglichen, die mit der Grenzstrommethode gemessen wurden. Dabei stellt man in einem Fehlerbereich von 20% gute Übereinstimmung fest.

ВЛИЯНИЕ ВНЕШНЕГО ЛАМИНАРНОГО ТЕЧЕНИЯ В КАНАЛЕ НА МАССООБМЕН ПОЛОСТИ

Аннотация—С помощью численного анализа при различных отношениях сторон, числах Рейнольдса и Шмидта изучалась интенсификация массообмена в полости за счет вихрей, обусловленных внешним течением в канале. С увеличением отношения сторон увеличивалось число вихрей, но только первичные и вторичные вихри способны были интенсифицировать массообмен. Среднее число Шервуда для каждого отношения сторон выражалось в виде $Sh_m = K\ Re^x\ Sc^y$. Сравнение результатов, полученных при отношении сторон, равном 1, с данными измерений по методу предельного тока показало их соответствие в пределах 20%.